

# Transfer-Enabled Fabrication of Graphene Wrinkle Arrays for Epitaxial Growth of AlN Films

Yuqing Song, Yaqi Gao, Xiaoting Liu, Jing Ma, Buhang Chen, Qin Xie, Xin Gao, Liming Zheng, Yan Zhang, Qingjie Ding, Kaicheng Jia, Luzhao Sun, Wendong Wang, Zhetong Liu, Bingyao Liu, Peng Gao, Hailin Peng, Tongbo Wei,\* Li Lin,\* and Zhongfan Liu\*

Formation of graphene wrinkle arrays can periodically alter the electrical properties and chemical reactivity of graphene, which is promising for numerous applications. However, large-area fabrication of graphene wrinkle arrays remains unachievable with a high density and defined orientations, especially on rigid substrates. Herein, relying on the understanding of the formation mechanism of transfer-related graphene wrinkles, the graphene wrinkle arrays are fabricated without altering the crystalline orientation of entire graphene films. The choice of the transfer medium that has poor wettability on the corrugated surface of graphene is proven to be the key for the formation of wrinkles. This work provides a deep understanding of formation process of transfer-related graphene wrinkles and opens up a new way for periodically modifying the surface properties of graphene for potential applications, including direct growth of AlN epilayers and deep ultraviolet light emitting diodes.

modify graphene properties, is promising for many applications.<sup>[3–6]</sup> In this regard, as an efficient approach to tune surface and optical properties,<sup>[3]</sup> and to alter the chemical reactivity due to the presence of strong strain,<sup>[7–9]</sup> graphene wrinkle can be formed by the collapsing or the folding of graphene geometrically.<sup>[10]</sup> Furthermore, free of dangling bonds, graphene is an ideal buffer layer for the epitaxial growth of functional materials, which is, however, strongly hindered by the difficulty of surface nucleation.<sup>[11,12]</sup> With enhanced reactivity, graphene wrinkles would function as the nucleation centers, and facilitate the rapid growth of epitaxial layers. Therefore, to periodically modify the properties and reactivity of graphene, the controllable

## 1. Introduction

Graphene has been attracting the academic and industrial interests owing to its promising properties and potential applications.<sup>[1,2]</sup> Patterning of graphene, which can periodically

formation of graphene wrinkle arrays with a high density and defined orientations is highly important. Applying the tension and compression loading<sup>[13,14]</sup> or substrate engineering<sup>[15,16]</sup> can be employed to fabricate the wrinkle arrays; however, the target substrates are limited to be the soft ones, such as polymer.

Y. Song, X. Liu, J. Ma, B. Chen, Q. Xie, X. Gao, L. Zheng, Y. Zhang, Q. Ding, K. Jia, L. Sun, Z. Liu, B. Liu, P. Gao, H. Peng, L. Lin, Z. Liu  
Beijing Graphene Institute (BGI)  
Beijing 100095, P. R. China  
E-mail: linli-cnc@pku.edu.cn; zfliu@pku.edu.cn

Y. Song, X. Liu, X. Gao, L. Zheng, K. Jia, Z. Liu, B. Liu, P. Gao, H. Peng, Z. Liu  
Center for Nanochemistry (CNC)  
College of Chemistry and Molecular Engineering  
Peking University  
Beijing 100871, P. R. China

Y. Gao, T. Wei  
Center of Materials Science and Optoelectronics Engineering University  
of Chinese Academy of Sciences  
Beijing 100049, P. R. China  
E-mail: tbwei@semi.ac.cn

Y. Gao, T. Wei  
Research and Development Center for Semiconductor Lighting  
Technology Institute of Semiconductors Chinese Academy of Sciences  
Beijing 100083, P. R. China

X. Liu, Q. Xie, X. Gao, Z. Liu, B. Liu, P. Gao  
Academy for Advanced Interdisciplinary Studies  
Peking University  
Beijing 100871, P. R. China

W. Wang  
Department of Physics and Astronomy  
University of Manchester  
Manchester M13 9PL, UK


Z. Liu, B. Liu, P. Gao  
Electron Microscopy Laboratory and International Center for Quantum  
Materials

School of Physics  
Peking University  
Beijing 100871, P. R. China

Z. Liu, B. Liu, P. Gao  
Collaborative Innovation Center of Quantum Matter  
Beijing 100871, P. R. China

Z. Liu, B. Liu, P. Gao  
Beijing National Laboratory for Molecular Sciences  
Beijing 100871, P. R. China

L. Lin  
Department of Materials Science and Engineering  
National University of Singapore  
Singapore 117575, Singapore

 The ORCID identification number(s) for the author(s) of this article can be found under <https://doi.org/10.1002/adma.202105851>.

DOI: 10.1002/adma.202105851

Recently, chemical vapor deposition (CVD) approaches have been widely used to produce large-area graphene films, and both the high-temperature growth and subsequent transfer process can produce wrinkles on rigid substrates.<sup>[17,18]</sup> The growth-related wrinkles are usually randomly orientated, while the transfer-related ones are still suffering from a low density.

Here, by unveiling the formation mechanism of transfer-related wrinkles, the successful fabrication of graphene wrinkle arrays on inch-sized SiO<sub>2</sub>/Si and sapphire substrates was achieved by using poly(propylene carbonate) (PPC)<sup>[19]</sup> as the transfer medium. The poor wettability of PPC on the corrugated surfaces of graphene on Cu ensures the presence of suspended graphene regions that are not supported by PPC during the transfer, which eventually leads to the formation of graphene wrinkles. The direction of wrinkle arrays was found to be determined by the orientation of the Cu step bunches (CuSBs), and the density of wrinkle can be as high as 10 wrinkles per μm<sup>2</sup>. The as-fabricated graphene wrinkle arrays would function as the buffer layers for the epitaxial growth of AlN, in which the presence of wrinkles would promote the nucleation and uniform growth of AlN with low strain level and improved lateral growth rates. Our work provides a deep understanding of formation mechanism of transfer-related graphene wrinkles and delivers a new approach for periodically altering the surface properties of graphene.

## 2. Results and Discussion

The conventional graphene transfer process should include the coating of the transfer medium on graphene surface, the delamination of graphene from the growth substrates, the lamination of graphene onto target substrates, and the removal of the transfer medium.<sup>[20]</sup> Owing to the high flexibility of graphene, the as-grown graphene would copy the surface structure of underlying Cu substrates to form a conformal contact. After the removal of Cu substrates, the graphene would only contact with the transfer medium. In this regard, the interfacial contact between the graphene and transfer medium after the removal of Cu would determine the formation of cracks and wrinkles.<sup>[10,21]</sup> In turn, the surface structure of Cu could influence the contact between graphene and transfer medium, because the initial structure of graphene would be determined by Cu.

We first investigate the relation between the Cu surface structure and the formation of transfer-related wrinkles. Usually, since the growth temperature of graphene is near the melting points of Cu, a corrugated surface with a high density of CuSBs is clearly visible in the atomic force microscopy (AFM) image of graphene on Cu directly after the CVD growth (Figure 1a; Figure S1, Supporting Information).<sup>[22]</sup> In detail, CuSBs appear periodically over the entire Cu surface, with an average density of 5 steps per μm<sup>2</sup> and an average step height of 15.0 nm. The CuSBs are usually well-oriented, and the orientation and symmetry are determined by the crystalline orientation of underlying Cu substrates.<sup>[22–24]</sup> To understand the role of Cu surface characteristics on the formation of wrinkles, we also grew ultra-flat graphene on sputtered single-crystal Cu on sapphire substrates without visible sharp Cu steps (Figure 1b). We transfer the different graphene samples using PPC as transfer medium.

Clearly, high-density graphene wrinkles were formed after transferring the graphene grown on corrugated Cu surfaces onto SiO<sub>2</sub>/Si substrates, and the graphene wrinkles exhibit a darker contrast in both optical microscopy (OM) (Inset, Figure 1c) and scanning electron microscopy (SEM) images (Figure 1c). Note that the formation of graphene wrinkle arrays is possible for PPC with different molecular weights (Figure S2, Supporting Information). Furthermore, inch-sized fabrication of graphene wrinkle arrays was achieved on SiO<sub>2</sub>/Si wafer and sapphire (Figure S3, Supporting Information). In clear contrast, almost no graphene wrinkles were observed when transferring the flat graphene grown on sputtered single-crystal Cu surface (Figure 1d). Further visualization of the graphene wrinkles was conducted by the AFM imaging. By carefully comparing the OM image (Figure S4, Supporting Information) and corresponding AFM images (Figure 1e; Figure S5, Supporting Information) of the same region, it was revealed that more graphene wrinkles which are invisible in OM images can be visualized by AFM imaging, and these wrinkles exhibited smaller widths than those of the optically visible wrinkles (Figure 1f). For the wrinkles invisible in OM image, the average width and height are 5–15 and 1–3 nm, while the average width is 40–160 nm and height is 3–8 nm for the optically visible wrinkles (Figure S6, Supporting Information). The density of wrinkles in the as-transfer graphene films from corrugated Cu surface is 10 wrinkles per μm<sup>2</sup>, which is clearly higher than the density of the wrinkles in the graphene films transferred from the flat Cu surface.

The folding of graphene films and the formation of wrinkles would lead to the accumulation of additional strains in graphene films. In this regard, we used the Raman spectroscopy to probe the spatial distribution of strains in as-received wrinkles arrays.<sup>[25]</sup> When graphene is subjected to the strain, the strain-induced anisotropy of the electron band structure and phonon dispersion can be well represented on its 2D peaks of the Raman spectra, by altering the bandwidth of the 2D peak.<sup>[26–28]</sup> Figure 1g shows typical Raman spectra of the regions with and without graphene wrinkles. Clearly, the full width at half maximum (FWHM) of 2D band of region in presence of wrinkles is 65 cm<sup>-1</sup>, higher than the 53 cm<sup>-1</sup> of flat graphene region, indicating the enhanced strain level in graphene wrinkles.<sup>[29]</sup> Figure 1h shows the corresponding Raman mapping of FWHM (2D), also confirming the enhanced strain level in the wrinkled regions (Figure 1h). In order to quantitatively determine the strain level, we plotted the corresponding 2D peak position ( $\omega_{2D}$ ) as a function of G peak position ( $\omega_G$ ) (Figure 1i). Owing to the different strain- and charge-sensitivity of  $\omega_G$  and  $\omega_{2D}$ , we can separate the strain and charge effects in graphene by the decomposition of strain and doping vectors, according to the previous report.<sup>[25]</sup> In detail, the fractional variation caused by the doping,  $(\Delta\omega_{2D}/\Delta\omega_G)_n$ , and the fractional variation caused by the strain,  $(\Delta\omega_{2D}/\Delta\omega_G)_e$ , is set to be 2.2 and 0.7, respectively, according to the reference.<sup>[25]</sup> Note that the  $\omega_G$  ( $1581.6 \pm 0.2$  cm<sup>-1</sup>) and  $\omega_{2D}$  ( $2676.9 \pm 0.7$  cm<sup>-1</sup>) of free-standing graphene (O) is used as the original point, which is free of additional charging and strain.<sup>[25]</sup> Therefore, it is possible to exact the strain level of every single point (P) by analyzing the projection of the vector (OP) on the line with slope of 2.2 (Figure 1i). Clearly, the results of flat graphene transferred from flat Cu

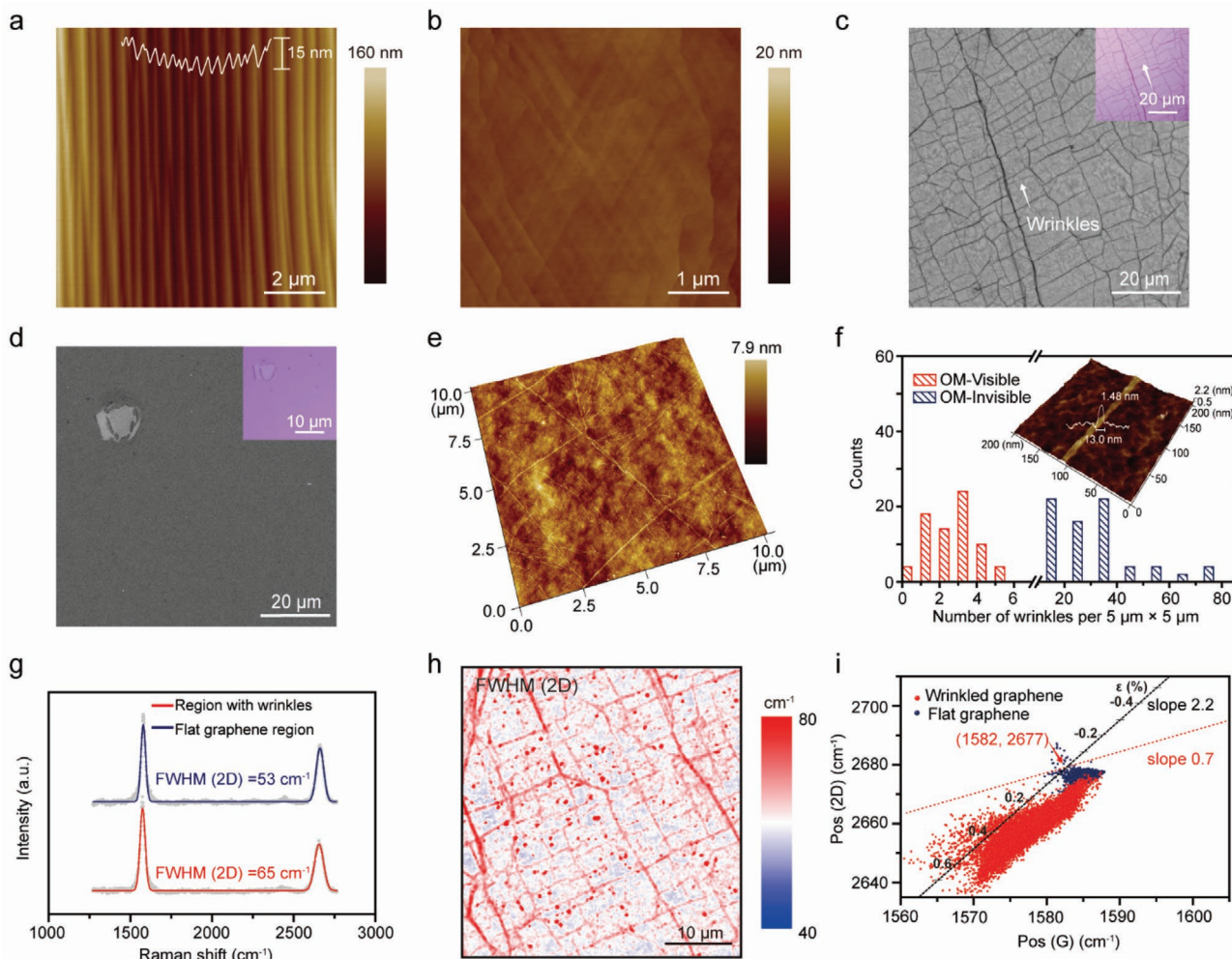


**Figure 1.** Preparation of transfer-induced graphene wrinkle arrays. a,b) AFM images of as-grown graphene films on Cu foil with CuSBs (a) and on flat Cu substrates (b). c,d) SEM images of as-transferred graphene films on SiO<sub>2</sub>/Si, which are grown on Cu foil with CuSBs (c) and on flat Cu substrates (d). Inset: corresponding OM images. The graphene crack in (d) is used to exhibit the contrast difference between graphene and substrates. e) Representative AFM image of as-received graphene wrinkle arrays transferred by using PPC as support layer. f) Statistics of the transferred graphene wrinkles that are visible in optical images (red), and detectable in AFM images. Each data was extracted from the OM image and corresponding AFM image of 5 × 5 μm<sup>2</sup> graphene transferred on SiO<sub>2</sub>/Si substrate. Inset: representative AFM image of wrinkles that is invisible in OM image but detectable in AFM imaging. g) Raman spectra of region with graphene wrinkles (red) and flat graphene region (blue). h) Raman mapping of FWHM of 2D band region of as-transferred graphene wrinkles. The locations of the wrinkle are clearly visible in Raman mapping. i) Correlation between the frequencies of the G and 2D peak positions of wrinkled (red), and flat graphene films (blue) that were prepared by the transfer of graphene grown on flat Cu surface. The data were obtained from corresponding Raman mapping results in (h). The black dot ( $\omega_G$  at 1582 cm<sup>-1</sup>,  $\omega_{2D}$  at 2677 cm<sup>-1</sup>) is the value for freestanding graphene taken from the literature.<sup>[25]</sup>

surface was closer to the result of free-standing graphene with a relatively low hole-doping, presumably owing to the water- and oxygen-doping introduced during the transfer. In contrast, the wrinkled graphene exhibited an enhanced level of strain. Assuming that the graphene undergoes biaxial strains, we calculated that the strain of wrinkled graphene range from 0.71% (tensile strain) to -0.07% (compressive strain).

The formation of graphene wrinkle arrays is highly related to the surface structures of Cu before the transfer. It was found that the choice of the transfer medium would also influence the wrinkle formation. The graphene films transferred with the assistance of polymethyl methacrylate (PMMA) exhibited a lower density of wrinkles than the density of wrinkles

in graphene films transferred by PPC (Figure S7, Supporting Information). To understanding the underlying reasons, after the coating of the transfer medium (PPC or PMMA) on graphene/Cu, we subsequently laminated thermal release tape (TRT) onto the surface of the polymer, and after the delamination of graphene from the Cu surfaces, we probed the surface structure of graphene on the transfer medium. Interestingly, when transferring graphene with the assistance of PMMA, the corrugated structure of graphene retains, while the corrugated structure disappears when PPC is used as transfer medium (Figure S8, Supporting Information). The ability to retain the surface structure indicates the conformal contact between graphene and PMMA. In contrast, the poor wettability of PPC

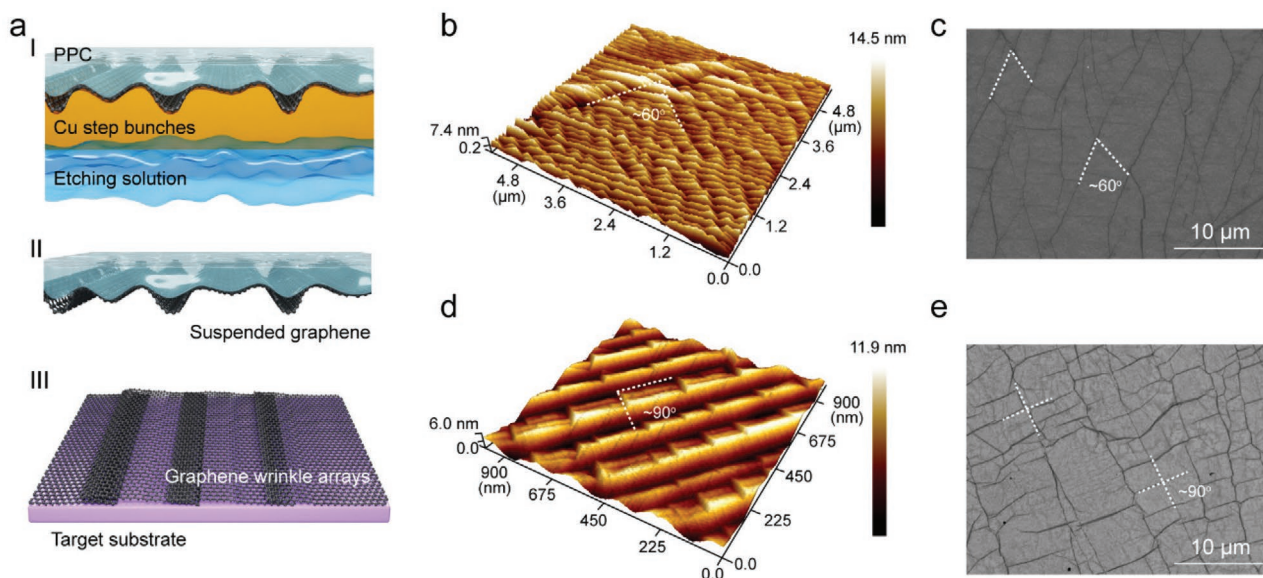


**Figure 2.** Formation mechanism of graphene wrinkle arrays. a) Schematic illustration of the formation mechanism of wrinkle arrays. The two reasons, growth of graphene on corrugated Cu surfaces and the poor wettability of PPC on the corrugated surfaces, contribute to the formation of graphene wrinkles. b) AFM image of as-grown graphene films on Cu (111) surface. c) SEM image of graphene wrinkle arrays with sixfold symmetry on SiO<sub>2</sub>/Si substrates transferred from Cu (111) crystal faces. d) AFM image of as-grown graphene films on Cu (100) surface. e) SEM image of graphene wrinkle arrays with fourfold symmetry on SiO<sub>2</sub>/Si substrates transferred from Cu (100) crystal faces.

on the surface of graphene would make the graphene partially suspended after the removal of supporting Cu substrates (Figure S9, Supporting Information). This would result in the disappearance of the corrugated Cu structure. Because the suspended graphene is more prone to be folded when undergoing the interfacial force, the presence of partially suspended graphene that is not supported by PPC would contribute to the formation of graphene wrinkles, especially when graphene is laminated onto the SiO<sub>2</sub>/Si substrates, as illustrated in Figure 2a.

Based on the above formation mechanism of graphene wrinkles, the symmetry and orientation of CuSBs would determine the corresponding symmetry and orientation of the graphene wrinkles. Taking Cu (111) and Cu (100) as examples: owing to the sixfold hexagonal symmetry of the Cu (111) surface, the as-formed Cu steps after the high-temperature surface reconstructions also exhibit a hexagonal symmetry, as evidenced by the AFM image of graphene grown on Cu(111) (Figure 2b).<sup>[30]</sup> In contrast, the AFM image of graphene grown on Cu (100) substrate indicates the presence of CuSBs with a fourfold symmetry (Figure 2d). We transferred both the graphene films grown on Cu (111) and Cu (100) onto the SiO<sub>2</sub>/Si substrate using PPC. The crystalline orientation of Cu (111) and Cu (100) foils was confirmed by electron backscatter diffraction (EBSD) measurements (Figure S10, Supporting Information). As expected, the symmetry of the wrinkles is consistent with the symmetry of CuSBs (Figure 2c,e), also confirming the contribution of Cu steps to the formation of wrinkles. Therefore, based on the above observations, we are capable of tuning the symmetry and orientation of graphene wrinkle array by growing graphene on different single-crystal Cu surfaces.<sup>[31]</sup> It can be also possible to engineer the wetting angle between graphene and PPC to achieve the controllability of graphene wrinkle arrays (Figure S11, Supporting Information).

High-resolution transmission electron microscopy (HR-TEM) imaging was conducted to probe the crystalline orientation of graphene wrinkle arrays. Both the graphene grown on Cu (111) and Cu (100) with corrugated surfaces were transferred to holey TEM grids using PPC as the transfer medium. As shown in the corresponding low-magnification TEM images (Figure 3a,b), the wrinkle arrays with six- and fourfold symmetry are formed on the as-transferred graphene films grown on Cu (111) and Cu (100) surface, respectively. We can locate the wrinkle based on the slight contrast difference in TEM images, which is caused by the layer number difference between graphene wrinkle and flat graphene region (Figure 3c), and the width of wrinkle is around 100 nm. To probe the lattice orientation of graphene wrinkle arrays, we carried out a series of selected area electron diffraction (SAED) measurements on points across the graphene wrinkles. Note that because the width of the graphene wrinkle is usually less than 100 nm, and the smallest size of the examined regions using SAED pattern is 200 nm, the SAED results of the wrinkled region should include the contribution from the nearby flat regions. Clearly, the patterns collected from the wrinkled region and nearby flat regions exhibit almost same orientation (Figure 3d–f), indicating that the formation of the wrinkles would not alter the crystalline orientation of the graphene film, and the single-crystal nature of entire graphene film retains. This conclusion is also supported by the high-angle annular dark-field scanning transmission electron microscopy (HAADF-STEM) observations (Figure 3g), where graphene on both sides of the wrinkle exhibit same lattice orientation in the atomically resolved images (Figure 3h,i; Figure S12, Supporting Information).

Using PPC as transfer medium, we prepared the graphene wrinkle arrays on sapphire substrates, so that graphene wrinkle arrays can function as the substrates for the epitaxial growth of

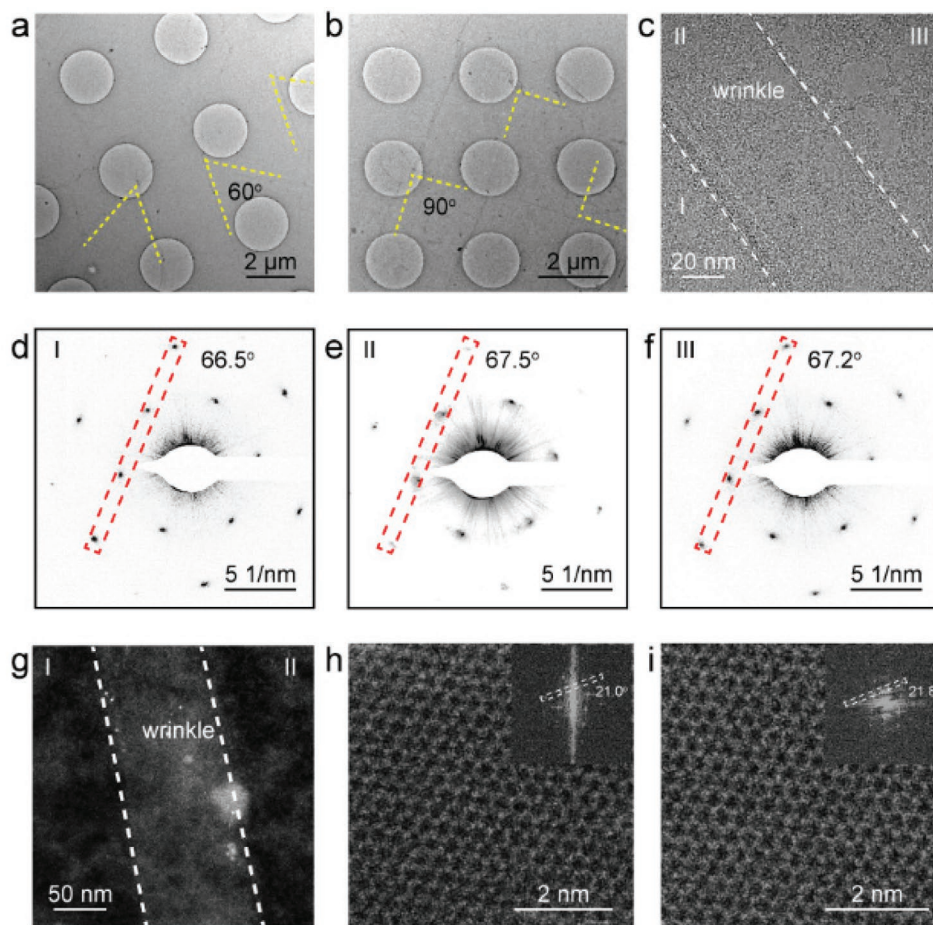


**Figure 3.** Crystalline orientation of graphene wrinkle arrays. a,b) Low-magnification TEM images of the graphene membrane transferred on a TEM grid. The graphene was grown on Cu (111) (a) and Cu (100) (b) surfaces, respectively. The dashed line highlights the angles of the as-formed wrinkles. c) High-magnification TEM image of graphene wrinkles, region I, III are flat graphene regions, while region II highlighted by the dash line is the graphene wrinkle with a little darker contrast. d–f) Corresponding SAED patterns results collected from the regions (I, II, III) shown in (c). The region in the presence of graphene wrinkles would contain more polymer residues in comparison with the flat region. This observation verifies that the polymer residues will influence the imaging quality of SAED patterns of graphene wrinkles. g) The HAADF-STEM image of wrinkle, while graphene wrinkle shows a lighter contrast. h,i) Corresponding HAADF-STEM images of the two marked regions (I, II) in (g), showing the atomic arrangement of graphene lattice. Inset of (h) and (i): Fast Fourier Transform (FFT) of the graphene with atomic resolution, revealing the similar graphene lattice direction on both sides of the graphene wrinkle.

AlN, which can be further used for the light-emitting diodes (LEDs)-based applications.<sup>[11]</sup> In this regard, graphene films, acting as buffer layers, can effectively release the strain in AlN to improve the performance of LEDs.<sup>[6]</sup> N<sub>2</sub> plasma pretreatment of graphene films was conducted to produce nucleation centers for the AlN growth.<sup>[32]</sup> Caused by the high strain level, the reactivity with the N<sub>2</sub> plasma would be highly enhanced in the presence of wrinkles. This would produce more nucleation centers to facilitate the nucleation of AlN epitaxial layer. The temporal evolution of the as-grown AlN epitaxial layer was presented in **Figure 4a–c**, where the different growth behaviors of AlN on the region in presence of graphene wrinkles, flat graphene region, and bare sapphire region are clearly observable. After 10 min growth of AlN, more AlN domains were formed on the region covered by graphene than those on bare sapphire regions, confirming the presence of graphene would enable the nucleation of AlN (**Figure 4a**; **Figure S13**, Supporting Informa-

tion). Furthermore, in graphene wrinkle region, the as-grown AlN domains nearly coalesced together, and the size of individual AlN domains exceed 500 nm. In clear contrast, the size of isolated AlN domains grown on flat graphene regions is limited to less than 200 nm, indicating the different lateral growth rates of AlN. This difference of growth rates should be caused by the enhanced adsorption of coming AlN particles owing to the presence of strain-rich wrinkles. After 20 min growth, a flat AlN film had been already formed on the region with graphene wrinkles, while in the flat graphene region, the coalescence of individual AlN domains into a flat film is still not observable (**Figure 4b**).

**Figure 4c** displays the change of the area ratio of the regions covered by AlN domains larger than 500 nm with the growth time, since the AlN domains would nearly laterally coalesced together to obtain a flat surface when their sizes exceed 500 nm. In detail, after 6 min growth, this area ratio in the region with

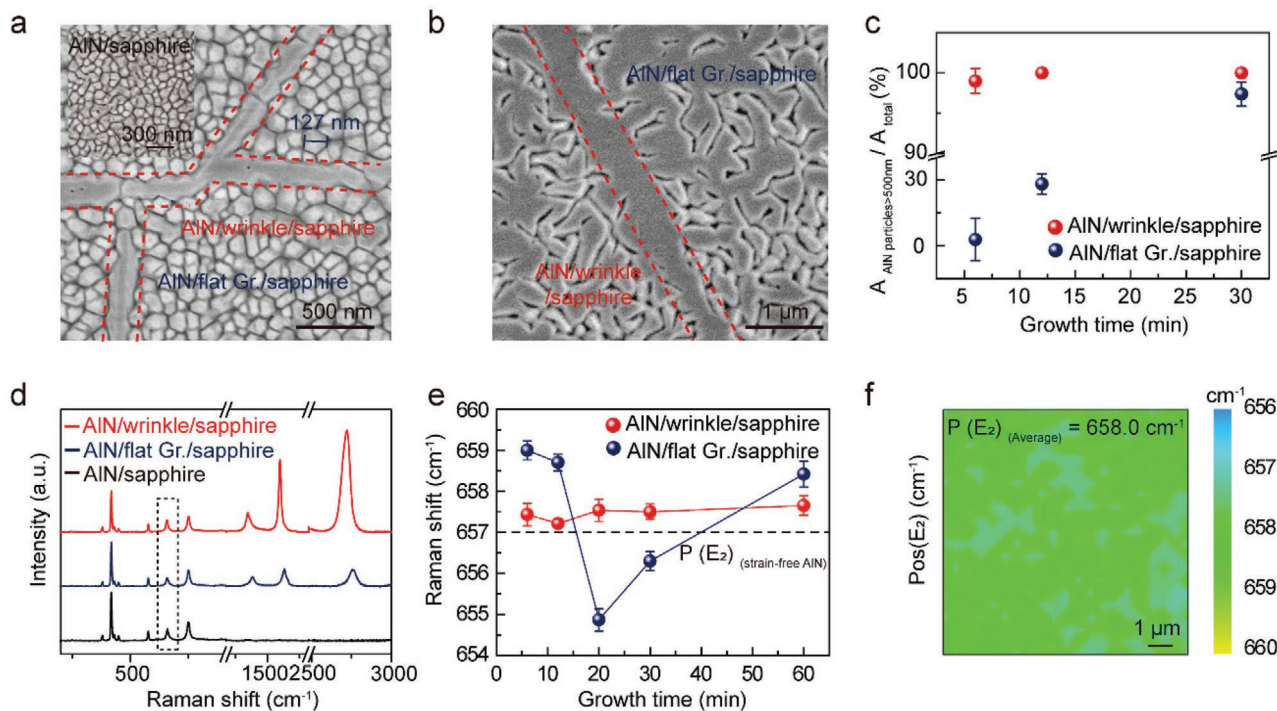


**Figure 4.** Effects of the graphene wrinkle arrays as buffer layer on the growth speed and strains in AlN. a) SEM image of the as-grown AlN on graphene wrinkle arrays after 10 min epitaxial growth of AlN. Clear, the AlN nearly fully cover the region with graphene wrinkles, in comparison with the region covered by graphene and bare sapphire region. The wrinkle region is highlighted by red dash line. Inset: SEM image of AlN domain grown on bare sapphire region. b) SEM image of the as-grown AlN on graphene wrinkle arrays after 20 min epitaxial growth of AlN. This observation indicated that the as-grown AlN epitaxial layer turn flat faster after 20 min growth, where other regions are still covered by isolated AlN domains without coalescence. c) Area ratio of regions covered by AlN domains larger than 500 nm as function as the growth time. Note than, the AlN domains would be coalesced together to obtain a flat surface, when their sizes exceed 500 nm. d) Raman spectra of flat region (blue), graphene wrinkles region (red), and bare sapphire region (black) after the 6 min epitaxial growth of AlN. e) Raman peak position of E<sub>2</sub> (high) of as-grown AlN on flat region (blue), graphene wrinkles region (red) at different growth times. f) Raman mapping of E<sub>2</sub> (high) peak position of graphene wrinkle arrays region after the 60 min epitaxial growth of AlN, which showed that, at a large scale, with the help of graphene wrinkle arrays the E<sub>2</sub> (high) peak of AlN was much closer to the pristine one compared to our previous work.<sup>[36]</sup>

the graphene wrinkles is 99.8% indicating the coalescence of nearby AlN domains, while the area ratio is only 2.8% in the flat graphene region. After the 12 min growth of AlN, the area ratio in wrinkled region arrived 100% indicating the full coalescence of AlN domains; however, this area ratio is still only 28.1% in flat graphene regions. Only after 30 min growth, it would arrive 100% in flat graphene region. The above observation indicates that the presence of wrinkles would facilitate the lateral growth of AlN and enable the fast coalescence of AlN domains to obtain a flat surface, which clearly highlighting the importance of preparing graphene wrinkle arrays for the epitaxial growth of AlN.

We used Raman spectroscopy to further evaluate the strain level of as-grown AlN films.<sup>[33]</sup> For AlN, the representative peaks are located around 248.0 cm<sup>-1</sup> (E<sub>2</sub> (low)), 657.0 cm<sup>-1</sup> (E<sub>2</sub> (high)), and 890.0 cm<sup>-1</sup> (A<sub>1</sub> (LO)), respectively.<sup>[34,35]</sup> The strain-sensitive E<sub>2</sub> (high) peaks in AlN/wrinkle/sapphire region were located at a wavenumber of ≈657.21 cm<sup>-1</sup>, much closer to bulk AlN (≈657.0 cm<sup>-1</sup>) and lower than that of AlN/flat graphene/sapphire (≈658.9 cm<sup>-1</sup>) and AlN grown on bare sapphire (≈661.2 cm<sup>-1</sup>) (Figure 4d). This demonstrates that the compressive strain in AlN was relaxed.

By carefully analyzing the wavenumbers of as-received AlN E<sub>2</sub> (high) peaks after different growth times, we found that the

E<sub>2</sub> (high) peak position of as-grown AlN on graphene wrinkle only exhibits minor changes during the entire 60 min growth, which suggests that the compressive strain in AlN is continuously relaxed during the growth process (Figure 4e). But for AlN on flat graphene, the strain of AlN evolved from the initial compressive strain (658.9 cm<sup>-1</sup>, 6 min) to the tensile strain (654.9 cm<sup>-1</sup>, 20 min), and finally to the compressive strain again (658.4 cm<sup>-1</sup>, 60 min) (Figure 4e; Figure S14, Supporting Information). It has been reported that the coalescence of AlN domains will introduce tensile strain, which is highly related to the corresponding AlN domain size.<sup>[36]</sup> The AlN domains formed on graphene wrinkles coalesced in the early growth stage; therefore the accumulation of the tensile strain caused by domain coalescence would be small in the subsequent growth process. In contrast, the coalescence of AlN domains on flat graphene region is not complete before 30 min growth, which would result in the accumulation of tensile strain. When the AlN film reaches a certain thickness, the tensile strain would be partially released by the formation of defects, such as dislocations. Furthermore, the compressive strain caused by thermal mismatch would be dominant after the formation of thick and flat AlN film. Therefore, the tensile strain of AlN films grown on flat graphene would be finally compensated by

the formation of dislocation and thermal mismatch. The corresponding Raman mapping (10  $\mu\text{m} \times 10 \mu\text{m}$ ) of the  $E_2$  (high) peak of as-grown AlN on graphene wrinkle arrays after 60-min growth shows that the  $E_2$  (high) peak of AlN is much closer to the pristine AlN compared to previous work.<sup>[37]</sup> Clearly, the formation of graphene wrinkle arrays would reduce AlN strain caused by the lattice and thermal mismatch between substrate and epitaxial layer.<sup>[16]</sup>

### 3. Conclusion

In summary, we have unveiled that the corrugated structure of as-grown graphene and the poor wettability of PPC on graphene surface would altogether enable the formation of graphene wrinkle arrays during the transfer process. The direction of wrinkle arrays can be determined by the atomic arrangement of Cu steps, and the density of the wrinkle can be improved to 10 wrinkles per  $\mu\text{m}^2$ . The crystalline orientation of the entire graphene films would retain after the formation of wrinkle arrays. Furthermore, as-received graphene wrinkle arrays would function as the buffer layer for the epitaxial growth of AlN, in which the fast lateral growth and coalescence of AlN epitaxial layer become possible. Our revelation of formation mechanism of transfer-related wrinkles would promote further research on the wrinkle-free transfer of graphene, as well as the periodic modification of graphene properties.

### 4. Experimental Section

**Preparations of CVD Graphene Membranes:** The high-temperature CVD growth of graphene films was carried out in a 6-inch quartz tube at low pressure. The heating-up and the annealing stage (1020  $^\circ\text{C}$ , 30 min) were both conducted under a flow of Ar (500 sccm, 1000 Pa), during which active site of Cu would be efficiently passivated for growing graphene films with larger domain sizes.

For CVD growth of graphene, the temperature was kept at 1020  $^\circ\text{C}$ . A gas mixture of  $\text{H}_2$  (500 sccm), Ar (500 sccm), and  $\text{CH}_4$  (0.8 sccm) was introduced into the hot zone to initiate the growth of graphene with a pressure of 1000 Pa. After 1 h of growth, the system was rapidly cooled to room temperature under the same atmosphere.

**PPC-Assisted Transfer of Graphene:** PPC-assisted transfer is composed of the following steps—(a) PPC (molecular weight, 50 000) was dissolved in anisole (a concentration of 0.1 g  $\text{mL}^{-1}$ ), and the received PPC solution was subsequently spin-coated on the top surface of CVD graphene films under spin coating rate of 1000 rpm for 60 s. Then, the PPC layer was cured at 60  $^\circ\text{C}$ , followed by the removal of the other side of the graphene by an  $\text{O}_2$  plasma etching. (b) The graphene films were floated on aqueous  $\text{Na}_2\text{S}_2\text{O}_8$  (1 Mol  $\text{L}^{-1}$ ) to etch away the Cu foils, followed by rinsing the films (PPC/graphene) with deionized (DI) water. (c) The target substrate ( $\text{SiO}_2/\text{Si}$  substrate) was then used to scoop the PPC-supported graphene films from deionized water. Subsequently, the as-received films drying at room temperature were conducted for more than 6 h to remove the water. (d) Finally, the PPC layer was removed by soaking the sample in an acetone bath, leaving behind graphene on the  $\text{SiO}_2/\text{Si}$  substrate after cleaning the sample with fresh acetone.

**Growth of Flat Single-Crystal Graphene Wafers:** Cu (111) single-crystal films were prepared by magnetron sputtering of Cu onto sapphire substrates ( $\alpha\text{-Al}_2\text{O}_3$  (0001)). In this regard, the main conditions include radio frequency (RF) power of 500 W, basal pressure of  $4 \times 10^{-4}$  Torr. Deposition time of 30 min is sufficient to obtain 500-nm-thickness of Cu film. Then, the Cu film was annealed in a high-temperature tubular

furnace to improve the crystalline quality. The annealing was conducted at atmospheric pressure under 500 sccm Ar and 10 sccm  $\text{H}_2$  gas, at 500  $^\circ\text{C}$  for 1 h. Further annealing at 1000  $^\circ\text{C}$  was subsequently carried out for 1 h. After the annealing of 1000  $^\circ\text{C}$ , the growth of graphene was initiated by introduction of a gas mixture of  $\text{H}_2$  (500 sccm), Ar (500 sccm), and  $\text{CH}_4$  (0.8 sccm), according to the reference.<sup>[14]</sup>

**PMMA-Assisted Transfer of Graphene:** The as-grown large-area graphene films on flat Cu wafers were transferred onto  $\text{SiO}_2/\text{Si}$  substrates using PMMA as transfer medium. (a) The PMMA (molecular weight, 996 000) was dissolved in anisole with a concentration of 4 mg  $\text{mL}^{-1}$ , and was spin coated on graphene surface under a spin coating rate of 2000 rpm  $\text{s}^{-1}$ . PMMA films were subsequently cured by heating the films at 170  $^\circ\text{C}$  for 3 min. (b) The Cu wafer was then etched away by an aqueous solution of  $(\text{NH}_4)_2\text{S}_2\text{O}_8$  (1 Mol  $\text{L}^{-1}$ ). (c) The PMMA/graphene stack was washed with deionized water, and placed on the  $\text{SiO}_2/\text{Si}$  substrate. (d) Finally, after the drying at atmosphere, the PMMA layer was removed by soaking the sample in acetone bath.

**AlN Growth:** The growth of AlN film was grown on surface of graphene using a low-pressure metalorganic chemical vapor deposition (MOCVD) ( $\approx 50$  Torr) at 1200  $^\circ\text{C}$ . Trimethylaluminum (70 sccm) and  $\text{NH}_3$  (500 sccm) were used as the Al and N precursors, and  $\text{H}_2$  (12 SLM) as the carrier gas. The growth is a one-step process, and the growth of AlN with 100-nm-thickness require 6 min while 1- $\mu\text{m}$ -thickness AlN need around 60 min growth.

**Characterization:** OM (Nikon Eclipse LV100), SEM (Hitachi S-4800, acceleration voltage 5–30 kV) were used to characterize the morphology and structure of the graphene films transferred onto a  $\text{SiO}_2$  (300 nm thick)/Si substrate. TEM images and SAED patterns were collected using FEI Tecnai F30 (at 300 keV electron energy) and an aberration-corrected TEM (Nion U-HERMES200; at 60 keV electron energy). AFM (Bruker dimension icon) was used to characterize the surface roughness of the graphene grown on Cu, and the graphene transferred onto the  $\text{SiO}_2/\text{Si}$  substrate with ScanAsyst mode. Raman characterization were conducted to analysis the strain and doping of graphene wrinkle array using Horiba, LabRAM HR-800, excited by a 532 nm laser.

### Supporting Information

Supporting Information is available from the Wiley Online Library or from the author.

### Acknowledgements

Y.S., Y.G., and X.L. contributed equally to this work. This work was financially supported by National Laboratory for Molecular Sciences (BNLMS- CXTD-202001) and Beijing Municipal Science & Technology Commission (Nos. Z181100004818001, Z191100000819005, Z19100000819007, and Z201100008720005), the National Basic Research Program of China (Nos. 2016YFA0200101, 2016YFA0200103, and 2019YFA0708203), and the National Natural Science Foundation of China (Nos. 21525310, 61974139, 51432002, and 51520105003). The authors acknowledge Electron Microscopy Laboratory of Peking University, China for the use of Cs corrected Nion U-HERMES200 scanning transmission electron microscopy.

### Conflict of Interest

The authors declare no conflict of interest.

### Data Availability Statement

Research data are not shared.

## Keywords

AlN, chemical vapor deposition, light emitting diodes, step bunches, transfer, wrinkle

Received: July 28, 2021

Revised: September 14, 2021

Published online: October 13, 2021

- [1] X. Li, W. Cai, J. An, S. Kim, J. Nah, D. Yang, R. Piner, A. Velamakanni, I. Jung, E. Tutuc, S. K. Banerjee, L. Colombo, R. S. Ruoff, *Science* **2009**, 324, 1312.
- [2] J. Song, F. Y. Kam, R. Q. Png, W. L. Seah, J. M. Zhuo, G. K. Lim, P. K. Ho, L. L. Chua, *Nat. Nanotechnol.* **2013**, 8, 356.
- [3] J. Zang, S. Ryu, N. Pugno, Q. Wang, Q. Tu, M. J. Buehler, X. Zhao, *Nat. Mater.* **2013**, 12, 321.
- [4] J. Bai, X. Zhong, S. Jiang, Y. Huang, X. Duan, *Nat. Nanotechnol.* **2010**, 4, 190.
- [5] A. Cagliani, D. M. A. Mackenzie, L. K. Tschammer, F. Pizzocchero, K. Almdal, P. Bøggild, *Nano Res.* **2014**, 7, 743.
- [6] N. Han, T. V. Cuong, M. Han, B. D. Ryu, S. Chandramohan, J. B. Park, J. H. Kang, Y. J. Park, K. B. Ko, H. Y. Kim, H. K. Kim, J. H. Ryu, Y. S. Katharria, C. J. Choi, C. H. Hong, *Nat. Commun.* **2013**, 4, 1452.
- [7] B. Deng, Z. Pang, S. Chen, X. Li, C. Meng, J. Li, M. Liu, J. Wu, Y. Qi, W. Dang, H. Yang, Y. Zhang, J. Zhang, N. Kang, H. Xu, Q. Fu, X. Qiu, P. Gao, Y. Wei, Z. Liu, H. Peng, *ACS Nano* **2017**, 11, 12337.
- [8] P. N. Nirmalraj, K. Thodkar, S. Guerin, M. Calame, D. Thompson, *npj 2D Mater. Appl.* **2018**, 2, 8.
- [9] S. Deng, D. Rhee, W. K. Lee, S. Che, B. Keisham, V. Berry, T. W. Odom, *Nano Lett.* **2019**, 19, 5640.
- [10] V. E. Calado, G. F. Schneider, A. M. M. G. Theulings, C. Dekker, L. M. K. Vandersypen, *Appl. Phys. Lett.* **2012**, 101, 103116.
- [11] H. Chang, Z. Chen, W. Li, J. Yan, R. Hou, S. Yang, Z. Liu, G. Yuan, J. Wang, J. Li, P. Gao, T. Wei, *Appl. Phys. Lett.* **2019**, 114, 091107.
- [12] H. Chang, B. Liu, D. Liang, Y. Gao, J. Yan, Z. Liu, Z. Liu, J. Wang, J. Li, P. Gao, T. Wei, *Appl. Phys. Lett.* **2020**, 117, 181103.
- [13] C. Androulidakis, E. N. Koukaras, M. G. Pastore Carbone, M. Hadjinicolaou, C. Galiotis, *Nanoscale* **2017**, 9, 18180.
- [14] Z. Li, I. A. Kinloch, R. J. Young, K. S. Novoselov, G. Anagnostopoulos, J. Parthenios, C. Galiotis, K. Papagelis, C. Y. Lu, L. Britnell, *ACS Nano* **2015**, 9, 3917.
- [15] W. K. Lee, J. Kang, K. S. Chen, C. J. Engel, W. B. Jung, D. Rhee, M. C. Hersam, T. W. Odom, *Nano Lett.* **2016**, 16, 7121.
- [16] D. Rhee, J. T. Paci, S. Deng, W. K. Lee, G. C. Schatz, T. W. Odom, *ACS Nano* **2020**, 14, 166.
- [17] N. Liu, Z. Pan, L. Fu, C. Zhang, B. Dai, Z. Liu, *Nano Res.* **2011**, 4, 996.
- [18] Z. Pan, N. Liu, L. Fu, Z. Liu, *J. Am. Chem. Soc.* **2011**, 113, 17578.
- [19] G. A. Luinstra, E. Borchardt, *Adv. Polym. Sci.* **2011**, 245, 29.
- [20] Y. Song, W. Zou, Q. Lu, L. Lin, Z. Liu, *Small* **2021**, 3, 2007600.
- [21] Y. C. Lin, C. C. Lu, C. H. Yeh, C. Jin, K. Suenaga, P. W. Chiu, *Nano Lett.* **2012**, 12, 414.
- [22] J. H. Kang, J. Moon, D. J. Kim, Y. Kim, I. Jo, C. Jeon, J. Lee, B. H. Hong, *Nano Lett.* **2016**, 16, 5993.
- [23] D. W. Kim, J. Lee, S. J. Kim, S. Jeon, H.-T. Jung, *J. Mater. Chem. C* **2013**, 1, 7819.
- [24] A. T. Murdock, A. Koos, T. B. Britton, L. Houben, T. Batten, T. Zhang, A. J. Wilkinson, R. E. Dunin-Borkowski, C. E. Lekka, N. Grobert, *ACS Nano* **2013**, 7, 1351.
- [25] J. E. Lee, G. Ahn, J. Shim, Y. S. Lee, S. Ryu, *Nat. Commun.* **2012**, 3, 1024.
- [26] J. Wu, H. Xu, J. Zhang, *Acta. Chim. Sin.* **2014**, 72, 301.
- [27] W. Hu, Z. Huang, Y. Zhou, W. Cai, J. Kang, *Sci. China Phys. Mech.* **2014**, 57, 2021.
- [28] M. Mohammadipour, A. Amoozadeh, *Chem. Mon.* **2017**, 148, 1075.
- [29] J. A. Robinson, C. P. Puls, N. E. Staley, J. P. Stitt, M. A. Fanton, *Nano Lett.* **2009**, 9, 964.
- [30] A. T. Murdock, A. Koos, T. B. Britton, L. Houben, T. Batten, T. Zhang, A. J. Wilkinson, R. E. Dunin-Borkowski, C. E. Lekka, N. Grobert, *ACS Nano* **2013**, 7, 1351.
- [31] Y. Li, L. Sun, Z. Chang, H. Liu, Y. Wang, Y. Liang, B. Chen, Q. Ding, Z. Zhao, R. Wang, Y. Wei, H. Peng, L. Lin, Z. Liu, *Adv. Mater.* **2020**, 32, 2002034.
- [32] H. Chang, Z. Chen, B. Liu, S. Yang, D. Liang, Z. Dou, Y. Zhang, J. Yan, Z. Liu, Z. Zhang, J. Wang, J. Li, Z. Liu, P. Gao, T. Wei, *Adv. Sci.* **2020**, 7, 2001272.
- [33] H. J. Trodahl, F. Martin, P. Murali, N. Setter, *Appl. Phys. Lett.* **2006**, 89, 061905.
- [34] M. Kadleikova, J. Breza, M. Vesely, *Microelectron. J.* **2001**, 32, 955.
- [35] V. Y. Davydov, Y. E. Kitaev, I. N. Goncharuk, A. N. Smirnov, J. Graul, O. Semchinova, D. Uffmann, M. B. Smirnov, A. P. Mirgorodsky, R. A. Evarestov, *Phys. Rev. B: Condens. Matter Mater. Phys.* **1998**, 58, 12899.
- [36] B. Sheldon, A. Bhandari, A. Bower, S. Raghavan, X. Weng, J. Redwing, *Acta Mater.* **2007**, 55, 4973.
- [37] Y. Qi, Y. Wang, Z. Pang, Z. Dou, T. Wei, P. Gao, S. Zhang, X. Xu, Z. Chang, B. Deng, S. Chen, Z. Chen, H. Ci, R. Wang, F. Zhao, J. Yan, X. Yi, K. Liu, H. Peng, Z. Liu, L. Tong, J. Zhang, Y. Wei, J. Li, Z. Liu, *J. Am. Chem. Soc.* **2018**, 140, 11935.